Computer Modeling in
Engineering & Sciences

Tech Science Press

https://doi.org/10.32604/cmes.2026.079927

ARTICLE

An Improved Support Vector Machine Method for Fault Diagnosis of Inter-Turn Short Circuit in PMSM with Enhanced Fault Representation

Yue Su[1], **Shukuan Zhang**[1,*], **Jinghao Jiao**[1], **Jiankang Zhong**[2] **and Qianxi Zhao**[1]

[1]College of Marine Electrical Engineering, Dalian Maritime University, Dalian, China
[2]Sichuan Key Technology Engineering Research Center for All-Electric Navigable Aircraft, Guanghan, Deyang, China

*Corresponding Author: Shukuan Zhang. Email: zhangshukuan@dlmu.edu.cn

Received: 30 January 2026; Accepted: 08 April 2026; Published: 27 April 2026

ABSTRACT: This paper introduces a novel dual-layer optimization fault diagnosis framework for inter-turn short-circuit (ITSC) faults in permanent magnet synchronous motors (PMSMs). The synergistic of a SABO-optimized VMD for enhanced feature extraction and an MFO-optimized SVM for intelligent classification is proposed. Firstly, mathematical and simulation models of ITSC faults in PMSMs are established to obtain fault phase currents and motor electromagnetic torques as characteristic fault signals. Then, the SABO algorithm is used to optimize the VMD parameters, followed by VMD decomposition of the characteristic fault signals to obtain Intrinsic Mode Functions (IMFs), and the time-domain parameters of the optimal IMF are calculated to obtain feature vectors. Finally, the fault type is predicted using an SVM optimized by the Moth-Flame Optimizer (MFO). Simulation results show that the accuracy of fault diagnosis can reach 93.6%, indicating that the proposed method can achieve accurate diagnosis of ITSC faults and effectively improve the accuracy of fault diagnosis.

KEYWORDS: Permanent magnet synchronous motor; inter-turn short circuit fault; support vector machine; fault diagnosis

1 Introduction

Permanent Magnet Synchronous Motors (PMSMs) are widely used in applications such as aerospace and industrial automation due to their high efficiency and torque density [1]. However, they are susceptible to inter-turn short circuit (ITSC) faults. Early detection is critical [2], as ITSC faults can lead to overheating, demagnetization, and eventual motor failure [3].

Existing diagnostic methods for ITSC faults fall into three main categories: signal-based, model-based, and artificial intelligence (AI)-based approaches. Among these, signal-based methods analyze fault-related physical signals such as motor current and temperature, and establish a mapping between extracted signal features and fault states to enable identification. For example, study [4] introduces a detection technique using reconstructed negative-sequence current and phase angle for ITSC faults in PMSMs, and study [5] proposes a diagnostic method based on subspace current residuals. While straightforward to implement, the effectiveness of signal-based approaches heavily depends on feature selection and extraction, which can be sensitive to external disturbances such as load variations, thereby compromising diagnostic robustness.

Model-based diagnosis involves establishing an analytical model of the motor under ITSC fault conditions and employing state or parameter estimation for fault identification. In [6], a fault diagnosis method is developed by modeling a multi-strand PMSM winding with ITSC faults. Similarly, in [7], a generalized predictive model for PMSM drives with inter-turn faults is established, incorporating torque ripple suppression into the diagnostic process. The accuracy of model-based methods depends on the precise acquisition of real-time motor parameters. However, motor parameters often vary nonlinearly under different operating conditions, making it difficult to establish an accurate analytical model and consequently restricting diagnostic precision.

In recent years, with the rapid advancement of AI algorithms, AI-based fault diagnosis has become a prominent research focus in motor condition monitoring. In [8], a multiscale channel attention-driven graph dynamic fusion network is proposed to realize robust fault diagnosis under noisy conditions. In [9], a hybrid learning framework combining genetic algorithm–optimized Morse wavelet time–frequency analysis and machine learning is proposed to diagnose single and combined motor faults. In [10], a recursive swarm decomposition technique with a two-layer decomposition framework and impulse-modulation energy score mode evaluation is proposed for efficient bearing fault detection and diagnosis. In [11], a class-aware supervised contrastive quadratic neural network is presented to achieve accurate and robust bearing fault diagnosis under industrial imbalanced data scenarios. The studies [12,13] propose two fault diagnosis methods using recurrent neural networks, which improve accuracy but involve complex hyperparameter tuning and high computational cost. In [14], a Transformer network is employed to evaluate ITSC fault severity in PMSMs, though the model is prone to local optima, affecting reliable fault identification. Support vector machines (SVMs), recognized for low computational complexity and strong robustness, have also been adopted in this field. In [15], a feature-based fault detection method using time–frequency analysis and SVM is proposed to realize early bearing fault diagnosis under varying operating conditions. The study [16] enhances conventional SVM with a genetic algorithm, and the study [17] integrates sparse representation with SVM to improve diagnostic accuracy. However, constructing an overcomplete dictionary in sparse representation remains challenging, and high training costs continue to limit practical deployment.

This paper introduces an optimized SVM-based method for ITSC fault diagnosis in PMSMs, with enhanced feature representation. First, a mathematical and simulation model of a PMSM under ITSC fault is developed to extract fault-phase currents and electromagnetic torque as characteristic signals. Next, since traditional variational mode decomposition (VMD) has limited adaptability when dealing with varying operating conditions and nonlinear variations in motor parameters, to address this, variational mode decomposition (VMD), optimized using the subtraction-average-based optimizer (SABO), is applied to construct discriminative feature vectors from the time-domain parameters of the optimal intrinsic mode function (IMF), thereby converting the fault information in massive original signals into nine indicators that can directly reflect fault severity, realizing enhanced fault feature representation and serving as the input data for the SVM model [18]. Finally, the moth–flame optimizer (MFO) is employed to tune the key parameters of the conventional SVM, yielding an MFO-SVM diagnostic model. The results indicate that the proposed method achieves higher diagnostic accuracy compared to existing approaches.

The main contribution of this research can be concluded that (1) An adaptive VMD is proposed to boost the adaptability corresponding to the input signals for refining the fault features extraction ability. (2) A dual-layer optimization framework combining SABO-VMD and MFO-SVM is proposed with adaptive parameter configuration introduced to both the fault feature extraction and classification diagnosis modules. This dual optimization overcomes limitations of empirical parameter selection in traditional methods, creating a robust and adaptive diagnostic framework.

2 Simulation Model for ITSC Fault

2.1 Mathematical and Simulation Models for ITSC Faults in PMSM

The equation for a PMSM in a healthy state in the abc coordinate system is

$$\boldsymbol{V}_{\mathrm{abc}} = R_{\mathrm{s}}\boldsymbol{i}_{\mathrm{abc}} + \frac{\mathrm{d}}{\mathrm{d}t}\left(\boldsymbol{L}_{\mathrm{s}}\boldsymbol{i}_{\mathrm{abc}} + \boldsymbol{\lambda}_{\mathrm{PM,abc}}\right) \tag{1}$$

where

$$\boldsymbol{V}_{\mathrm{abc}} = \begin{bmatrix} V_{\mathrm{a}} & V_{\mathrm{b}} & V_{\mathrm{c}} \end{bmatrix}^{\mathrm{T}} \tag{2}$$

$$\boldsymbol{i}_{\mathrm{abc}} = \begin{bmatrix} i_{\mathrm{a}} & i_{\mathrm{b}} & i_{\mathrm{c}} \end{bmatrix}^{\mathrm{T}} \tag{3}$$

$$\boldsymbol{\lambda}_{\mathrm{PM,abc}} = \begin{bmatrix} \lambda_{\mathrm{PM,a}} & \lambda_{\mathrm{PM,b}} & \lambda_{\mathrm{PM,c}} \end{bmatrix} \tag{4}$$

$$\boldsymbol{L}_{\mathrm{s}} = \begin{bmatrix} L & M & M \\ M & L & M \\ M & M & L \end{bmatrix} \tag{5}$$

where $\boldsymbol{V}_{\mathrm{abc}}$ denotes the three-phase voltage; R_{s} represents the phase resistance; $\boldsymbol{i}_{\mathrm{abc}}$ signifies the three-phase current; $\boldsymbol{L}_{\mathrm{s}}$ is the phase inductance; L is the self-inductance of each phase winding; M indicates the mutual inductance between two-phase windings; and $\lambda_{\mathrm{PM,abc}}$ corresponds to the three-phase permanent magnet flux linkage.

The short-circuit turn ratio μ is defined as shown in Eq. (6).

$$\mu = \frac{n}{N} \tag{6}$$

where n represents the number of short-circuited turns in the faulted phase, N denotes the total number of turns in that phase, R_{f} signifies the residual insulation resistance between the two short-circuited turns when R_{f} is sufficiently large, the motor is fault-free; when R_{f} equals 0, there is a complete short-circuit between the turns. i_{f} stands for the current in the short-circuited branch. The effects of core magnetic saturation and other nonlinear factors are neglected, leading to the following equation:

$$\boldsymbol{V}_{\mathrm{abcf}} = \boldsymbol{R}_{\mathrm{sf}}\boldsymbol{i}_{\mathrm{abcf}} + \frac{\mathrm{d}}{\mathrm{d}t}\left(\boldsymbol{L}_{\mathrm{sf}}\boldsymbol{i}_{\mathrm{abcf}} + \boldsymbol{\lambda}_{\mathrm{PM,abcf}}\right) + \boldsymbol{V}_{0,\mathrm{abcf}} \tag{7}$$

where

$$\boldsymbol{V}_{\mathrm{abcf}} = \begin{bmatrix} V_{\mathrm{a}} & V_{\mathrm{b}} & V_{\mathrm{c}} & 0 \end{bmatrix}^{\mathrm{T}} \tag{8}$$

$$\boldsymbol{i}_{\mathrm{abcf}} = \begin{bmatrix} i_{\mathrm{a}} & i_{\mathrm{b}} & i_{\mathrm{c}} & i_{\mathrm{f}} \end{bmatrix}^{\mathrm{T}} \tag{9}$$

$$\boldsymbol{R}_{\mathrm{sf}} = \begin{bmatrix} R_{\mathrm{s}} & 0 & 0 & -\mu R_{\mathrm{s}} \\ 0 & R_{\mathrm{s}} & 0 & 0 \\ 0 & 0 & R_{\mathrm{s}} & 0 \\ \mu R_{\mathrm{s}} & 0 & 0 & -\mu R_{\mathrm{s}} - R_{\mathrm{f}} \end{bmatrix} \tag{10}$$

$$\boldsymbol{L}_{\mathrm{sf}} = \begin{bmatrix} L & M & M & -\mu L \\ M & L & M & -\mu M \\ M & M & L & -\mu M \\ \mu L & \mu M & \mu M & -\mu^2 L \end{bmatrix} \tag{11}$$

$$\boldsymbol{\lambda}_{\mathrm{PM,abcf}} = \begin{bmatrix} \lambda_{\mathrm{PM,a}} & \lambda_{\mathrm{PM,b}} & \lambda_{\mathrm{PM,c}} & \lambda_{\mathrm{PM,f}} \end{bmatrix}^{\mathrm{T}} \tag{12}$$

$$\boldsymbol{V}_{0,abcf} = \begin{bmatrix} V_0 & V_0 & V_0 & 0 \end{bmatrix}^{\mathrm{T}} \tag{13}$$

Establish a simulation model for ITSC faults in PMSM, as shown in Fig. 1. Assume that the fault occurs in phase B. The parameters of the PMSM in the ITSC fault simulation model are listed in Table 1.

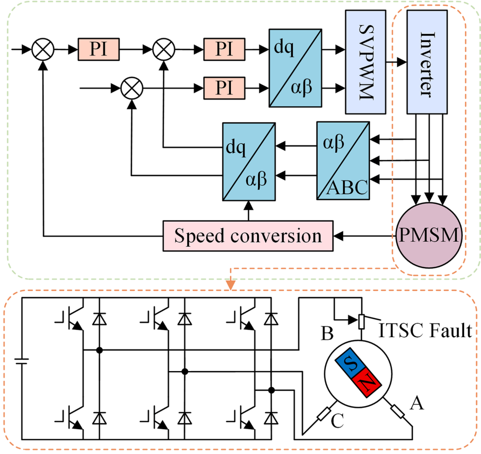

Figure 1: PMSM simulation model.

Table 1: Model parameters of PMSM.

Parameter	Value
Stator resistance (Ω)	0.6123
Phase inductance (mH)	5.25
Rotor flux linkage (Wb)	0.1827
Moment of inertia (kg·m^2)	0.03
Rated speed (r·min^{-1})	1000
Number of pole pairs	3

2.2 Simulation of PMSM ITSC Fault

According to Eq. (6), parameter n is proportional to μ. Therefore, the adjustment of n can be directly realized by varying μ, meaning that the setting of n is essentially equivalent to that of μ. In this paper, the range of μ investigated is from 0 to 0.45, which is divided into five intervals corresponding to different fault severities, namely (0, 0.05), [0.05, 0.15), [0.15, 0.25), [0.25, 0.35), and [0.35, 0.45), as summarized in Table 2. To more accurately simulate the gradual transition from mild to severe faults, enhance the completeness of the experimental design, and improve the algorithm's generalization ability and recognition stability under various fault degrees, multiple gradient values of μ are selected within each interval during simulation. For instance, in the interval [0.35, 0.45), five fault conditions are specified with μ equals 0.35, 0.375, 0.4, 0.42, and 0.44.

To analyze the variation patterns of electromagnetic torque and phase current in a PMSM under different degrees of ITSC faults, simulations were conducted for the five fault labels previously defined. Using the median μ value of each fault interval as a representative case, the electromagnetic torque and phase current under healthy and faulty conditions are shown in Figs. 2 and 3, respectively. From 0 to 0.3 s, the motor starts and operates normally. From 0.3 to 0.8 s, ITSC fault labels 1 to 5 are applied sequentially. As shown in Fig. 2, under healthy conditions the torque remains stable around 50 N·m with small fluctuations. As the ITSC fault severity increases, the torque oscillates more noticeably around 50 N·m, with increasingly prominent pulsations. Fig. 3 shows that under healthy operation the three-phase currents are symmetrical and equal in amplitude. With progressively severe ITSC faults, current symmetry deteriorates and form distortion becomes more pronounced. Both electromagnetic torque and phase current carry characteristic information useful for ITSC fault diagnosis. However, these signals are susceptible to noise and external interference, which can obscure fault features. Therefore, further signal processing is necessary to enhance the detectability of fault characteristics.

Table 2: Fault labels of ITSC of PMSM.

μ	Fault Location	ITSC Fault Label
(0, 0.05)	Phase B	1
[0.05, 0.15)	Phase B	2
[0.15, 0.25)	Phase B	3
[0.25, 0.35)	Phase B	4
[0.35, 0.45)	Phase B	5

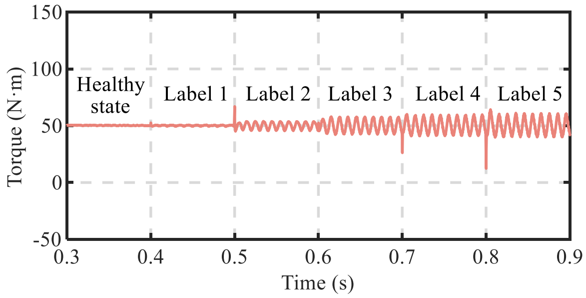

Figure 2: Electromagnetic torque of PMSM under ITSC fault.

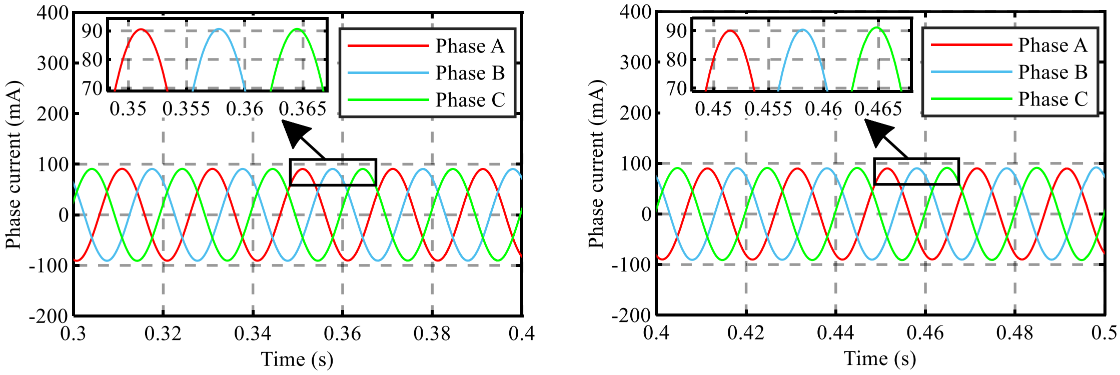

(a) (b)

Figure 3: (Continued)

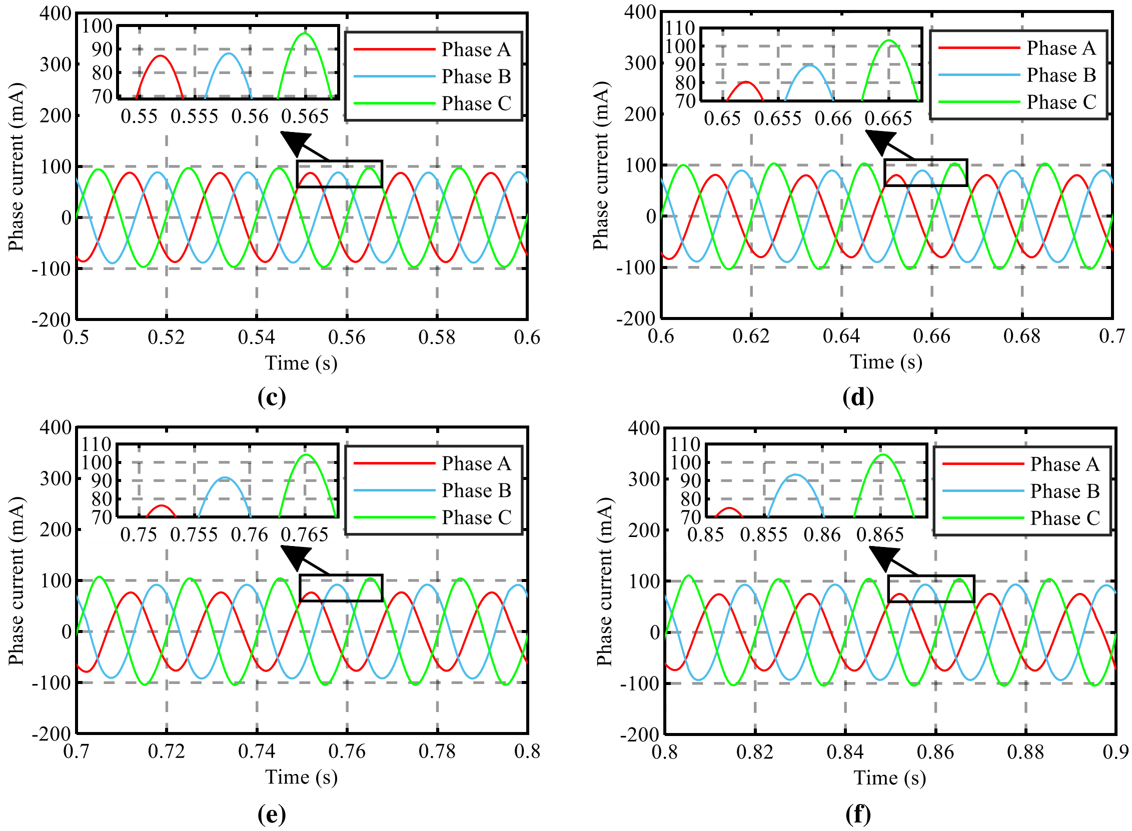

(c) (d) (e) (f)

Figure 3: PMSM phase current under ITSC fault: (**a**) Healthy state. (**b**) Label 1. (**c**) Label 2. (**d**) Label 3. (**e**) Label 4. (**f**) Label 5.

3 SABO-VMD Fault Feature Extraction Method

3.1 VMD Parameter Optimization Method Based on SABO

VMD is a method for separating non-stationary frequency signals based on a variational optimization framework. It can decompose the signal to be decomposed into several strictly orthogonal IMF components, reducing the blurring effect of noise on fault features and enhancing the clarity and distinguish ability of fault features.

Assuming the signal is decomposed into k IMF components, a constrained variational model is established.

$$\min_{\{u_k\},\{\omega_k\}} \left\{ \sum_k \left\| \partial t \left[\left(\delta(t) + \frac{j}{\pi} \right) u_k(t) \right] e^{-j\omega_k t} \right\|_2^2 \right\} \tag{14}$$

$$s.t. \sum\nolimits_k u_k = f \tag{15}$$

where t denotes time, f is the original signal, u_k represents the modal function, ∂t signifies the gradient operation, $\delta(t)$ is the impulse function, ω_k stands for the actual center frequency of each mode, $e^{-j\omega kt}$ corresponds to the estimated center frequency of each analytical signal, $j^2 = -1$, $\|\cdot\|_2$ denotes the L_2 norm, *s.t.* indicates the constraint condition, and $\sum_k u_k$ represents the summation of all modal components.

Before using the VMD algorithm, it is essential to select an appropriate number of modes, denoted as K, and a penalty factor, denoted as α. A value of K that is too large can lead to over-decomposition, whereas a value that is too small can result in under-decomposition. Similarly, an α value that is too large can cause the loss of frequency band information, while a value that is too small can result in information redundancy. Therefore, accurately determining the optimal parameter combination $[K, \alpha]$ is crucial for the successful decomposition of VMD.

SABO is an optimization algorithm based on the subtraction and average operators. As it only adopts arithmetic mean and v-subtraction operations and updates only with the single parameter of search agent displacement, it avoids complex function calculations and excessive parameters used in common optimizers such as GWO and PSO. Therefore, the SABO algorithm has higher computational efficiency. Meanwhile, when updating the positions of search agents, the SABO algorithm performs v-subtraction for each agent in the search space, which makes full use of the information of all individuals. Compared with other common optimization methods that only rely on optimal individual information, the SABO algorithm can escape from local optima more easily and achieve higher optimization accuracy. Accordingly, it is designed to efficiently identify optimal VMD parameters by minimizing a quantitative metric, thereby ensuring that the resulting IMFs exhibit strong noise immunity, rich feature content, and high inter-mode distinguish ability. As a single-metric fitness function may inadequately characterize the IMFs, this paper introduces a composite index γ—formulated from permutation entropy and mutual information entropy—to jointly evaluate the noise level and feature richness of the decomposed components. Since a lower γ value corresponds to less noise interference and richer feature information, minimizing γ is adopted as the fitness function. The composite index γ and the fitness function F are defined as follows:

$$\gamma = H_P/\overline{M} \tag{16}$$

$$F = \min_{1\sim K}\{C\} \tag{17}$$

where H_P denotes the permutation entropy of the input signal, and $\overline{M}$ represents the normalized mutual information.

To further demonstrate the superiority of the composite indicator selected as the fitness function in this paper, a fault sample belonging to the first fault type with a short-circuit turns ratio of 0.03 is input into SABO-VMD for decomposition. Envelope entropy, permutation entropy, and the composite indicator are respectively used as the fitness functions for SABO to compare their corresponding fitness values. Among these, envelope entropy measures the complexity of the signal envelope; a smaller value indicates more pronounced impact characteristics and more prominent fault information. Information entropy quantifies the complexity of the signal; a smaller value reflects stronger signal regularity and lower uncertainty. As analyzed above, a smaller value of the composite indicator is also preferable; therefore, the optimal parameter combination should minimize the fitness function value. The comparison results are shown in Fig. 4.

As can be seen from Fig. 4, the composite indicator achieves the smallest fitness function value of 0.0025151, which is more than two orders of magnitude lower than that obtained by envelope entropy and more than three orders of magnitude lower than that obtained by information entropy. This indicates that the composite indicator selected in this paper is the most suitable fitness function, enabling a superior VMD parameter combination and achieving better fault feature decomposition.

The pseudo-code table for optimizing VMD parameters using the SABO algorithm is shown in Algorithm 1. Initially, the VMD parameters to be optimized, namely the mode number K and the penalty factor α, are provided as inputs to the SABO algorithm. The SABO parameters are then initialized, including the maximum number of iterations N, the bounds for the penalty factor α_b and the mode number K_b, as well as the dimension of the optimization variables D. Subsequently, the fitness function F is formulated, and the fitness values for all search agents are evaluated. These search agents are updated following Eq. (20). The process continues until the maximum iteration count is reached, at which point the near-optimal solutions for K and α are returned as output.

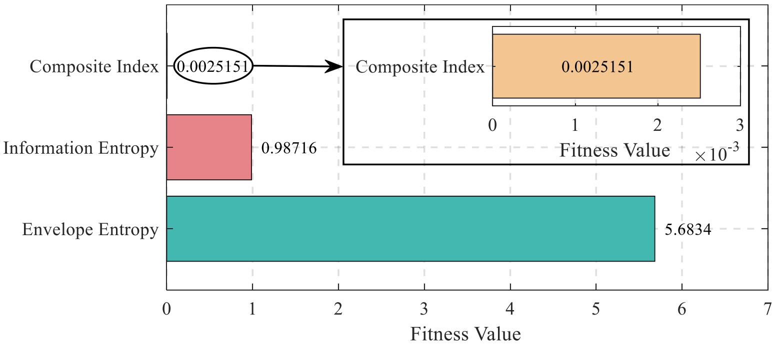

Figure 4: Comparison of fitness values obtained with different fitness functions.

In Algorithm 1, $r_{i,d}$ is a random number within the interval [0, 1]; lb_d and ub_d represent the lower and upper bounds of the d-th decision variable, respectively, corresponding to the lower and upper bounds of the K and α search intervals; X_i^{new} denotes the new suggested position of the i-th search agent; N signifies the total number of search agents; r_i is a vector with a dimension of m, whose elements follow a normal distribution within the interval [0, 1]; F_i^{new} and F_i represent the fitness function values of the search agent X_i^{new} and X_i, respectively.

Algorithm 1: Subtraction average based optimizer (SABO)

```
Input VMD information: number of modes $K$ and penalty factor $\alpha$, and constraints $\alpha_b$ and $K_b$
Set SABO population size ($N$) and iterations ($T$)
Randomly generate the matrix of initial search agents using equation:
    $x_{i,d} \leftarrow lb_d + r_{i,d} \cdot (ub_d - lb_d)$
Set objective function $F$
Evaluate the objective function
for $t = 1, T$ do
    for $i = 1, N$ do
        Determine the proposed new position of the $i$-th SABO search agent using equation:
            $X_i^{\text{new}} = X_i + \vec{r} * \frac{1}{N} \sum_{d=1}^{N} (X_i - vX_d), i = 1, 2, \ldots, N$
        Update $i$-th population member using equation:
            $X_i = \begin{cases} X_i^{\text{new}}, F_i^{\text{new}} < F_i \\ X_i, \text{else} \end{cases}$    (20)
    end for
    Save the best candidate solution so far
end for
Output the best quasi-optimal solution obtained with SABO
```

3.2 Fault Feature Extraction Based on SABO-VMD

To improve the fault diagnosis performance of the SVM classification model, the data input to the model should contain sufficient and effective fault features. Therefore, it is crucial to perform enhanced fault feature representation on the original fault signals.

To achieve this, the SABO-VMD fault feature extraction method is employed to decompose the fault phase current and electromagnetic torque of the PMSM, resulting in K IMFs with different central frequencies. For each IMF component obtained by decomposition, using the defined fitness function F, the IMF with the lowest fitness function value among the K IMFs is selected as the optimal value, and its time-domain parameters are used to construct a feature vector, thereby converting massive original fault signals into discriminative indicators that effectively quantify fault severity, which serves as the dataset for the input layer of the fault diagnosis model.

The feature vector needs to possess both high sensitivity to impactful fault signals and strong robustness against external interference factors. This paper integrates the dimensionless time-domain parameters and dimensioned time-domain parameters to construct the feature vector.

Dimensionless parameters, including peak factor, pulse factor, margin factor, form factor, and kurtosis factor, are normalized metrics that exhibit high sensitivity to signal waveform variations and shape characteristics. These parameters are inherently robust against amplitude scaling and baseline drift because they depend on the relative proportions of signal features rather than absolute magnitudes. For instance, the kurtosis factor effectively captures impulsive components induced by ITSC faults while remaining insensitive to uniform gain variations caused by sensor calibration errors or load fluctuations. Conversely, dimensioned parameters, including root-mean-square (RMS) value, mean value, peak value, and variance, provide absolute quantitative measures that reflect the actual energy content and magnitude of fault signals. These parameters are essential for distinguishing between different severity levels of ITSC faults, as the absolute current amplitude and torque magnitude directly correlate with the short-circuit turn ratio μ.

This paper constructs a feature vector with 18 dimensions, integrating the fault characteristics of motor fault phase current and electromagnetic torque. The process of the SABO-VMD fault feature extraction method is shown in Fig. 5. Firstly, fault phase current and electromagnetic torque are obtained from the PMSM as the original fault data set. Then, the original fault data undergoes SABO-VMD decomposition to obtain IMFs, and the IMF with the smallest fitness function value is selected as the optimal IMF. Finally, nine time-domain parameters are extracted from the optimal IMF of fault phase current and the optimal IMF of electromagnetic torque, respectively, to construct an 18-dimensional feature vector.

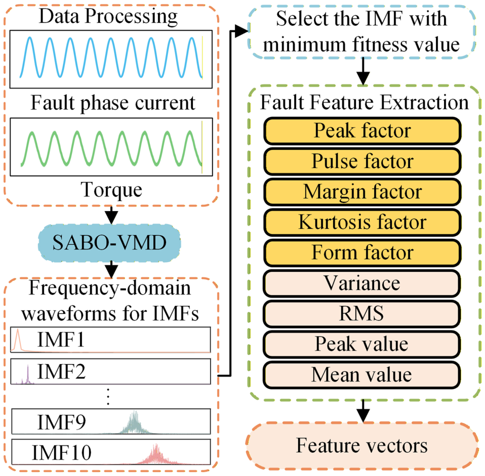

Figure 5: SABO-VMD fault feature extraction method process.

4 Fault Diagnosis Based on MFO-SVM

4.1 Optimization of SVM Parameters Based on MFO

SVM is a supervised learning algorithm based on the VC dimension and structural risk minimization principle, possessing excellent generalization ability and adaptability to high-dimensional data. The classification performance of SVM is closely related to the selection of kernel function and parameter configuration. The RBF kernel function, with its powerful nonlinear mapping capability and high flexibility, is chosen as the kernel function for SVM. It is crucial to set the corresponding penalty factor C and RBF kernel function parameter σ to reduce the fitting error and computational complexity of the model, which is key to optimizing the performance of SVM.

The MFO algorithm, inspired by the natural phenomenon of moth phototaxis, is an intelligent optimization algorithm characterized by fast search speed and strong optimization capability. MFO adopts a spiral update mechanism that searches for better solutions along the spiral path while approaching the optimal solution, making it easier to escape local optima. In comparison, GWO mainly searches the region surrounded by the current top three optimal solutions. Although it includes random components, its exploration capability is limited compared to MFO's spiral mechanism, making GWO more prone to local optima. PSO relies on velocity-position updates and tends to oscillate near the optimal solution due to velocity residue, resulting in low convergence accuracy. Therefore, MFO demonstrates superior optimization accuracy, and this paper selects it for SVM parameter optimization. The process of optimizing SVM parameters using MFO is shown in Fig. 6.

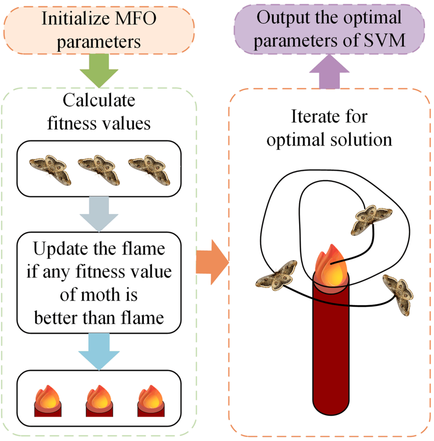

Figure 6: Specific process of MFO optimizing SVM parameters.

As shown in Fig. 6, moths search around the current optimal flame with a logarithmic spiral trajectory. The large spiral radius allows them to approach the flame while exploring better solutions nearby. At the end of each iteration, the algorithm sorts moths and flames by fitness, updates flames with optimal individuals, and guides moths to search around new flames. This spiral updating mechanism enables the MFO algorithm to effectively avoid local optima. Furthermore, in highly complex motor fault scenarios, the search space of the algorithm contains numerous local optimal solutions, which severely interfere with the search for the global optimum. Therefore, the ability of the algorithm to effectively avoid local optima in complex environments with a large number of local optimal solutions is crucial. Among the CEC2005 test functions, F8–F13 are multimodal functions with an exponential number of local optima, and their optimization characteristics are highly consistent with highly complex motor fault scenarios. According to [19], the MFO algorithm exhibits significantly superior optimization performance on the test functions F8, F10, F11, and F13 compared with competing algorithms such as PSO. It only fails to achieve the optimal results on F9 and F12, and this disadvantage is statistically significant only on F9. Accordingly, the MFO algorithm can effectively avoid falling into local optima under complex fault conditions with dense local optimal solutions.

Firstly, input the SVM parameters to be optimized and initialize the MFO parameters, including the maximum iteration count T, population size N, and search range of the parameters to be optimized. Then, calculate the fitness function values of each moth and flame. To reflect the impact of different combinations of C and σ obtained during the iteration process on the diagnostic accuracy of the SVM diagnostic model, this paper selects the average error rate of 5-fold cross-validation of SVM prediction results as the fitness function value. When the fitness function value of any moth is better than that of a certain flame, the moth becomes a new flame, the original flame is eliminated, and the iteration continues to search for the optimal solution. Finally, when the iteration count reaches the maximum iteration count T, the optimal C and σ found are output for use in the ITSC fault diagnosis model.

4.2 ITSC Fault Diagnosis Method Based on Improved SVM

The flowchart of the improved SVM method for fault diagnosis of ITSC in PMSMs with enhanced fault features, constructed in this paper, is shown in Fig. 7. The method is generally divided into two stages: enhanced feature extraction and intelligent optimization diagnosis. Firstly, the SABO-VMD is utilized to perform adaptive decomposition on the fault current and torque signals, extracting sensitive time-domain features to construct enhanced feature vectors. Subsequently, an MFO-optimized SVM classifier is employed to identify and classify the fault type, thereby achieving accurate and rapid intelligent diagnosis of ITSC in PMSMs. The ITSC fault diagnosis model constructed in this paper exhibits high accuracy, capable of detecting ITSC in PMSMs within 0.5 s of the fault occurrence and providing the range of the short-circuited turn ratio. This combined model can detect faults in a timely manner, reduce fault damage, and provide detailed fault data information for subsequent fault maintenance.

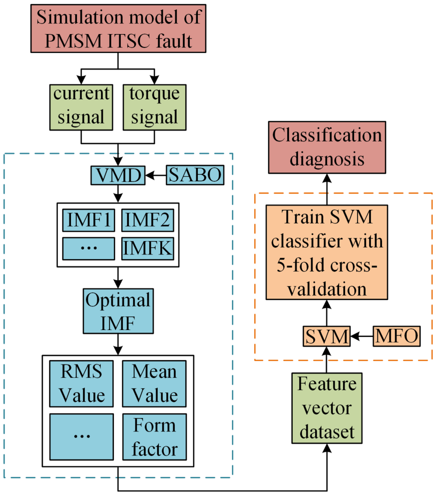

Figure 7: The process of improved SVM ITSC fault diagnosis method.

5 Diagnosis and Analysis of ITSC Fault in PMSM

5.1 Analysis of SABO-VMD Feature Extraction Effectiveness

Among the five parameters of SABO, the population size N and the maximum iteration count T play a crucial role in the algorithm's performance. If T is too small, the algorithm's convergence accuracy will be low; if T is too large, it will lead to a decrease in iteration efficiency. If N is too small, it will result in insufficient search; if N is too large, it will lead to a waste of computational resources and a decrease in efficiency. Taking into account both the algorithm's convergence accuracy and computational efficiency, the parameters of the SABO algorithm are determined as shown in Table 3.

Table 3: Configuration of SABO-optimized VMD parameters.

N	T	α_b	K_b	D
15	20	[100, 2500]	[3, 10]	2

To more intuitively demonstrate the optimization effect of SABO on traditional VMD decomposition, this section takes the fault phase current at $\mu = 0.32$ as an example. Figs. 8 and 9 respectively list the frequency domain forms of each IMF obtained through traditional VMD decomposition and SABO-VMD decomposition. The traditional VMD parameters are set as $K = 6$ and $\alpha = 1000$. After SABO parameter optimization, the optimal parameter combination $[K, \alpha]$ for SABO-VMD is [10, 2324]. As shown in Fig. 8, the frequency domain forms of each IMF obtained through traditional VMD decomposition exhibit a wide-frequency distribution, with mode mixing phenomenon, making fault features easily mixed with other frequency components, and the distinction between each IMF is insufficient. As shown in Fig. 9, the frequency domain forms of each IMF obtained through SABO-VMD decomposition exhibit a narrow-band distribution, with strong frequency concentration, and the distinction between each IMF is high. This avoids the occurrence of mode mixing phenomenon in traditional VMD, enhances the representation of fault features, and verifies the effectiveness of the SABO-VMD joint feature extraction method.

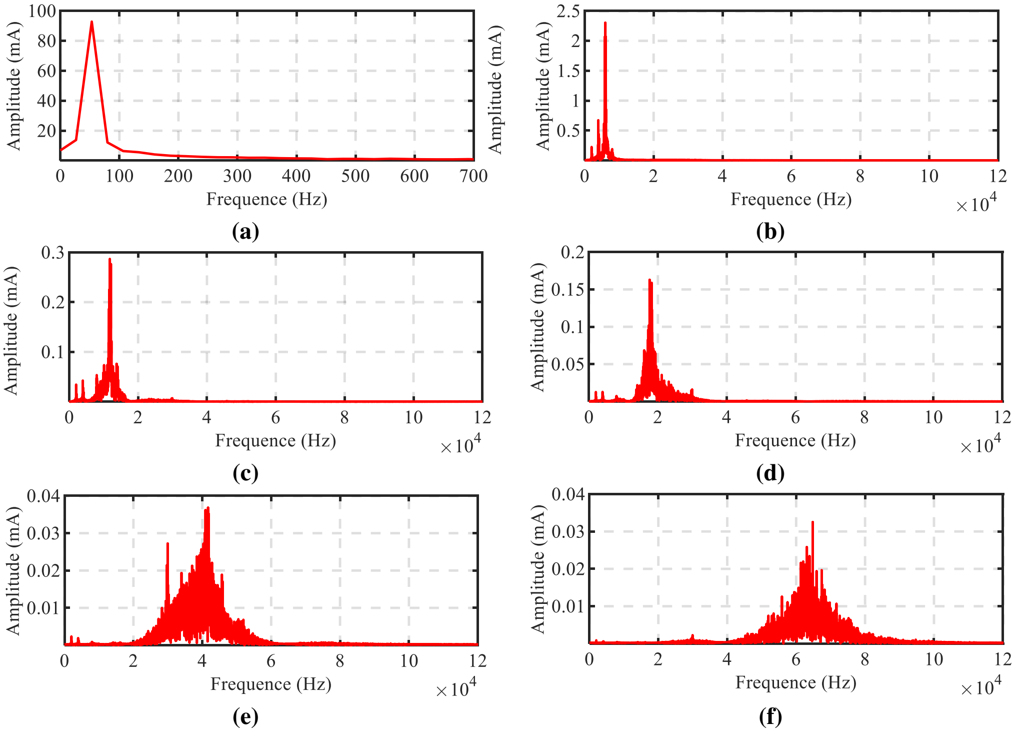

Figure 8: Frequency domain forms of each IMF decomposed by VMD: (**a**) IMF1. (**b**) IMF2. (**c**) IMF3. (**d**) IMF4. (**e**) IMF5. (**f**) IMF6.

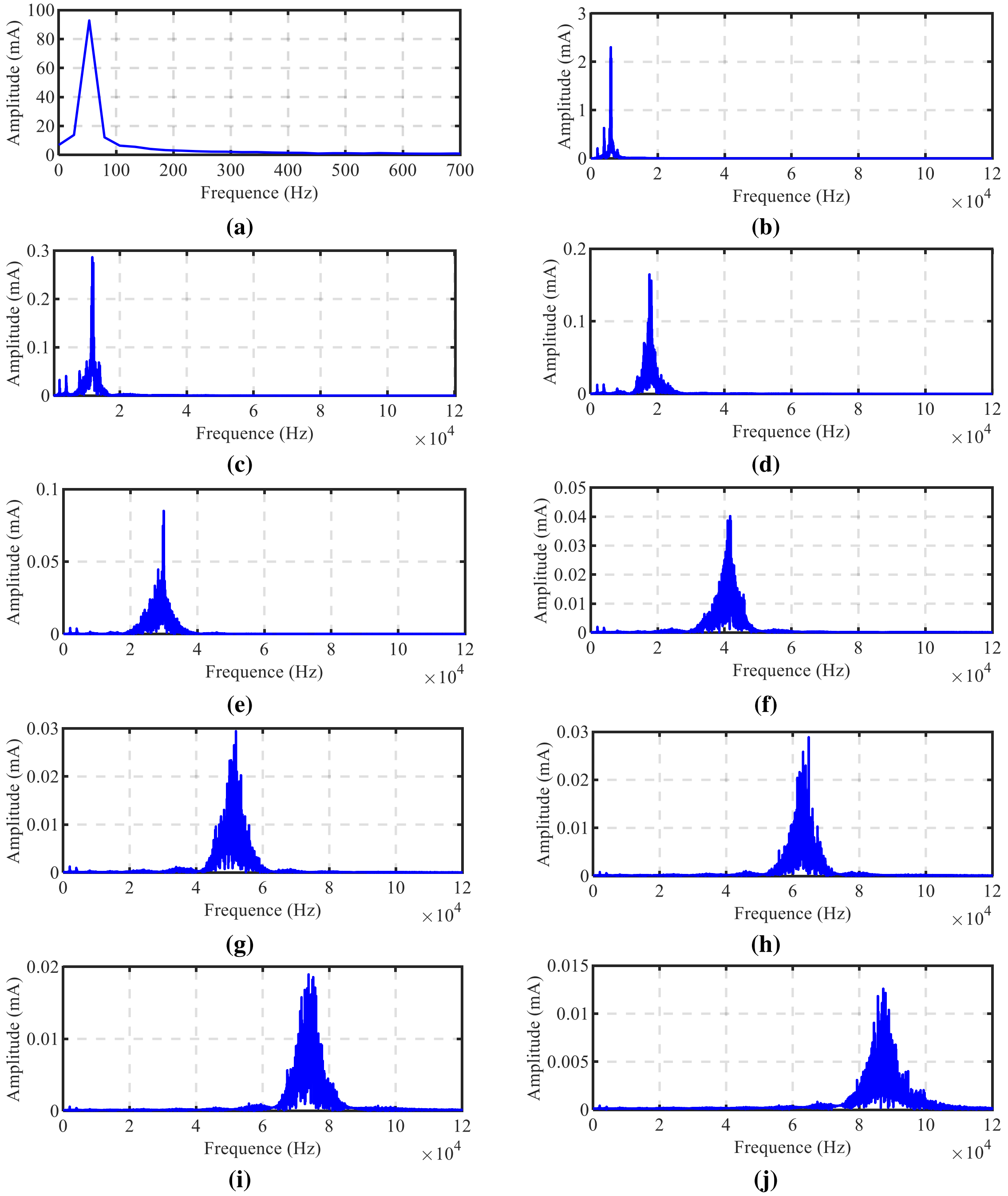

Figure 9: Frequency domain forms of each IMF decomposed by SABO-VMD: (**a**) IMF1. (**b**) IMF2. (**c**) IMF3. (**d**) IMF4. (**e**) IMF5. (**f**) IMF6. (**g**) IMF7. (**h**) IMF8. (**i**) IMF9. (**j**) IMF10.

5.2 Analysis of MFO-SVM Fault Diagnosis Results

To quantify the performance of the SVM fault diagnosis model, mean squared error (*MSE*) and correlation coefficient (*R*) are selected as indicators. The smaller the *MSE* and the closer *R* is to 1, the better the prediction performance of the SVM model. *MSE* and *R* can be expressed as follows:

$$MSE = \frac{1}{m}\sum_{i=1}^{m}\left(y_i' - y_i\right)^2 \tag{18}$$

$$R = \sqrt{\frac{\left(m\sum_{i=1}^{m} y_i' y_i - \sum_{i=1}^{m} y_i' \sum_{i=1}^{m} y_i\right)^2}{\left[m\sum_{i=1}^{m} y_i' - \left(\sum_{i=1}^{m} y_i'\right)^2\right]\left[m\sum_{i=1}^{m} y_i^2 - \left(\sum_{i=1}^{m} y_i\right)^2\right]}} \tag{19}$$

where m represents the size of the training set.

This study compares the fault diagnosis performance of the MFO-optimized SVM model with that of the baseline SVM model without parameter optimization. Both models were trained and tested on the same dataset, with the MFO algorithm configured with a population size of 40 and a maximum of 100 iterations. The comparative results are presented in Fig. 10. The MFO-SVM model achieves an R-value of 0.99 and a low MSE of 0.038 on the training set. On the test set, it maintains a high R-value of 0.96 and an MSE of 0.16, demonstrating strong fitting ability and reliable pattern recognition. In contrast, the baseline SVM model yields R-values of 0.87 (training) and 0.84 (test), which are 12.1% and 12.5% lower, respectively, than those of the MFO-SVM model. Correspondingly, its MSE values reach 0.52 and 0.65—significantly higher than those obtained by the optimized model. These results confirm that the MFO-SVM fault diagnosis model outperforms the original SVM model in both predictive accuracy and generalization capability.

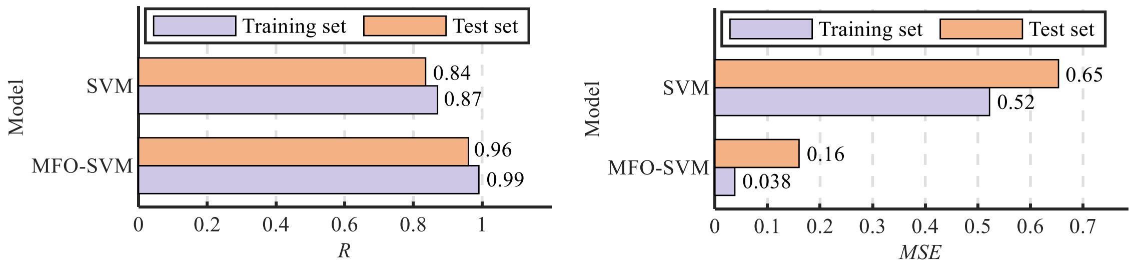

(a) **(b)**

Figure 10: Comparison of MFO-SVM and SVM performance: (**a**) *R*. (**b**) *MSE*.

5.3 Comparative Analysis of Different Methods

To verify the effectiveness and superiority of the proposed method, this paper selects the widely used Particle Swarm Optimizer (PSO) and Grey Wolf Optimizer (GWO) to optimize the original SVM model, and compares the MFO-SVM fault diagnosis model proposed in this paper with the GWO-SVM and PSO-SVM fault diagnosis results. The population size of all three algorithms is 40, the maximum number of iterations is 100, and the input dataset remains consistent. The model test results are shown in Table 4.

The F1 score is an indicator of a model's classification performance, with a higher F1 score indicating stronger classification performance. As can be seen from Table 4, the F1 score of the MFO-SVM model can reach 0.936, which is higher than that of the GWO-SVM model and the PSO-SVM model. This proves that the MFO-SVM model has the strongest generalization ability and stronger classification and diagnosis performance for fault data compared to the other two optimization models.

In terms of diagnostic accuracy, the MFO-SVM model achieves a fault diagnosis accuracy of 93.6%, which demonstrates the effectiveness of the proposed method. Furthermore, compared with the GWO-SVM and PSO-SVM models, the MFO-SVM model improves diagnostic accuracy by 2.0% and 34%, respectively, demonstrating its performance advantage and further validating the superiority of the proposed approach.

Table 4: Comparison of test results for three models.

Model	F1 Score	Diagnostic Accuracy (%)
MFO-SVM	0.936	93.6
GWO-SVM	0.916	91.6
PSO-SVM	0.621	59.6

From the perspective of individual fault categories, Table 5 presents a comparison of the per-class classification accuracies of the three models across five fault types. Specifically, for Label 1, both MFO-SVM and GWO-SVM achieve a diagnostic accuracy of 1.00, whereas PSO-SVM attains only 0.52. For Label 5, MFO-SVM significantly outperforms the other two models with a high accuracy of 0.98. In the cases of Label 2, Label 3, and Label 4, MFO-SVM yields accuracies of 0.94, 0.92, and 0.84, respectively. Although its accuracy is slightly lower than that of GWO-SVM for Labels 2 and 4, it still maintains a relatively high level of classification precision. In contrast, PSO-SVM exhibits consistently low accuracy across categories, with a maximum value of only 0.84, revealing a substantial performance gap compared to the other two optimized models.

Table 5: Comparison of class-wise accuracy for three models.

Model	Label 1	Label 2	Label 3	Label 4	Label 5
MFO-SVM	1.00	0.94	0.92	0.84	0.98
GWO-SVM	1.00	0.96	0.92	0.88	0.82
PSO-SVM	0.52	0.84	0.52	0.54	0.56

To visually represent the distribution of correct and incorrect diagnostic results, Fig. 11 lists the confusion matrices of the three fault diagnosis models. As can be seen from Fig. 11, the MFO-SVM classification model proposed in this paper exhibits the highest recognition accuracy across the five fault categories, with only a small number of fault label prediction errors. Among the 250 samples, the MFO-SVM model, GWO-SVM model, and PSO-SVM model misclassify 16, 21, and 101 samples, respectively.

The superior performance of the MFO-SVM model over other fault diagnosis models is closely related to the update mechanism of the MFO algorithm. Different from the GWO algorithm, which primarily relies on the enclosure spanned by the three optimal individuals for local exploitation and only occasionally explores new regions through the divergence mechanism, and the PSO algorithm, which updates the particle positions relying on velocity iteration, the MFO algorithm adopts a spiral update mechanism. In this mechanism, individuals approach the current optimal solution along a logarithmic spiral trajectory and explore other potential superior positions on the spiral path simultaneously. Compared with GWO and PSO, MFO presents stronger global search capability and more effective local contraction. This update mechanism not only ensures sufficient global exploration but also achieves satisfactory local exploitation, thus effectively preventing the algorithm from falling into local optima. Therefore, MFO exhibits higher convergence accuracy in optimizing the key parameters of SVM, enabling the MFO-SVM model to achieve better fault diagnosis performance.

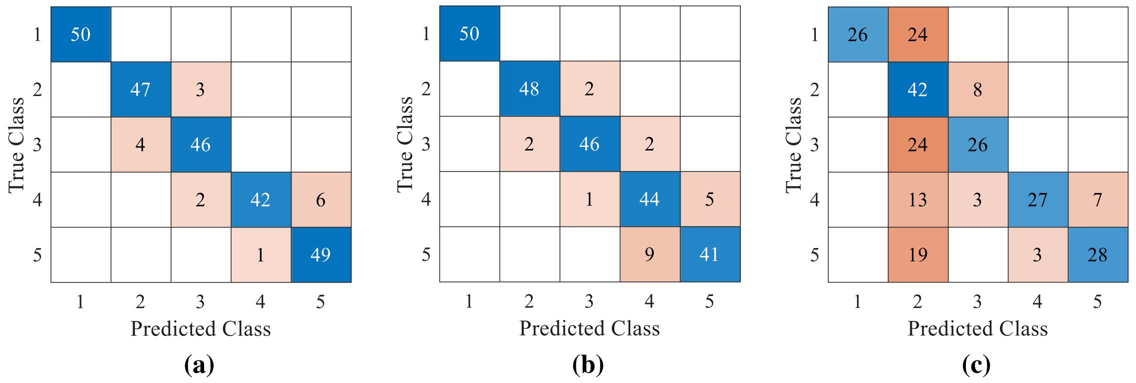

Figure 11: Confusion matrices of SVM models optimized by different algorithms: (**a**) MFO-SVM. (**b**) GWO-SVM. (**c**) PSO-SVM.

6 Conclusion

This paper proposes an enhanced SVM method for diagnosing ITSC faults in PMSMs, which incorporates an improved fault feature representation. Specifically, VMD optimized by the SABO is applied to extract discriminative fault features from the fault-phase current and electromagnetic torque signals, enhancing the characterization of ITSC faults. Furthermore, a fault diagnosis model termed MFO-SVM is developed by optimizing SVM parameters with the MFO, which improves diagnostic performance. The proposed method achieves an ITSC fault diagnosis accuracy of 93.6%. Comparative experiments with SVM models optimized by other algorithms confirm the superiority of the presented approach.

Acknowledgement: Not applicable.

Funding Statement: This work was supported in part by the Basic Research Project of Liaoning Provincial Department of Education under Grant LJ212510151015, in part by the Sichuan Province All-Electric Navigation Aircraft Key Technology Engineering Research Center under Grant CAFUC2025KF03.

Author Contributions: Conceptualization, Shukuan Zhang; methodology, Yue Su and Shukuan Zhang; software, Yue Su, Jinghao Jiao and Qianxi Zhao; validation, Yue Su and Jinghao Jiao; formal analysis, Yue Su and Qianxi Zhao; investigation, Yue Su, Jinghao Jiao and Jiankang Zhong; data curation, Yue Su, Jinghao Jiao and Qianxi Zhao; writing—original draft preparation, Yue Su and Shukuan Zhang; writing—review and editing, Yue Su, Shukuan Zhang and Jiankang Zhong; visualization, Yue Su and Qianxi Zhao; supervision, Shukuan Zhang and Jiankang Zhong; project administration, Shukuan Zhang; funding acquisition, Yue Su, Shukuan Zhang and Jiankang Zhong. All authors reviewed and approved the final version of the manuscript.

Availability of Data and Materials: Data available on request from the authors.

Ethics Approval: Not applicable.

Conflicts of Interest: The authors declare no conflicts of interest.

References

1. Qin L, Jiang Z, Xing X, Wang X, Yin Y, Zhou Y, et al. Non-singular fast terminal sliding mode control of PMSM based on disturbance observer. Comput Mater Contin. 2025;83(3):5279–98. doi:10.32604/cmc.2025.063358.
2. Khawaja AU, Shaf A, Al Thobiani F, Ali T, Irfan M, Pirzada AR, et al. Optimizing bearing fault detection: CNN-LSTM with attentive TabNet for electric motor systems. Comput Model Eng Sci. 2024;141(3):2399–420. doi:10.32604/cmes.2024.054257.

3. Delgado Prieto M, Garcia Espinosa A, Riba Ruiz JR, Urresty JC, Ortega JA. Feature extraction of demagnetization faults in permanent-magnet synchronous motors based on box-counting fractal dimension. IEEE Trans Ind Electron. 2011;58(5):1594–605. doi:10.1109/TIE.2010.2066538.
4. Li D, Zhu M, Zhao Y, Lin S. Detection and location of inter-turn short circuit fault in PMSM based on reconstructed negative sequence current and phase angle. J Electr Eng Technol. 2025;20(6):4243–55. doi:10.1007/s42835-025-02289-0.
5. Hang J, Wang X, Li W, Ding S. Interturn short-circuit fault diagnosis and fault-tolerant control of DTP-PMSM based on subspace current residuals. IEEE Trans Power Electron. 2025;40(2):3395–404. doi:10.1109/TPEL.2024.3484469.
6. Qian H, Guo H, Ding X. Modeling and analysis of interturn short fault in permanent magnet synchronous motors with multistrands windings. IEEE Trans Power Electron. 2016;31(3):2496–509. doi:10.1109/TPEL.2015.2439574.
7. Li W, Hang J, Ding S, Wang Q. Common predictive model for PMSM drives with interturn fault considering torque ripple suppression. IEEE Trans Transp Electrif. 2023;9(3):4071–9. doi:10.1109/TTE.2022.3232820.
8. Zhang X, Liu J, Zhang X, Lu Y. Multiscale channel attention-driven graph dynamic fusion learning method for robust fault diagnosis. IEEE Trans Ind Inform. 2024;20(9):11002–13. doi:10.1109/TII.2024.3397401.
9. Rahmatullah R, Serteller NFO, Ak A. Hybrid learning framework for motor fault diagnosis *via* optimized wavelet-based time–frequency analysis and deep feature classification. IEEE Access. 2026;14:38604–19. doi:10.1109/ACCESS.2026.3672016.
10. Xing X, Wang W, Melek W. A new swarm decomposition technique for bearing fault detection and diagnosis. IEEE Trans Instrum Meas. 2026;75:3508213. doi:10.1109/TIM.2026.3667340.
11. Yu WE, Zhang S, Sun J, Li C, Liao JX, Zhang X. A class-aware supervised contrastive quadratic neural network for imbalanced bearing fault diagnosis. IEEE Trans Reliab. 2026;75:1266–80. doi:10.1109/TR.2026.3668191.
12. Lee H, Jeong H, Koo G, Ban J, Kim SW. Attention recurrent neural network-based severity estimation method for interturn short-circuit fault in permanent magnet synchronous machines. IEEE Trans Ind Electron. 2021;68(4):3445–53. doi:10.1109/TIE.2020.2978690.
13. Lan Q, Chen B, Yao B. A novel motor fault diagnosis method based on generative adversarial learning with distribution fusion of discrete working conditions. Comput Model Eng Sci. 2023;136(2):2017–37. doi:10.32604/cmes.2023.025307.
14. Parvin F, Faiz J, Qi Y, Kalhor A, Akin B. A comprehensive interturn fault severity diagnosis method for permanent magnet synchronous motors based on transformer neural networks. IEEE Trans Ind Inform. 2023;19(11):10923–33. doi:10.1109/TII.2023.3242773.
15. Mehmeti X, Karahoda B. Efficient intelligent early bearing fault detection with frequency of high-frequency band time–frequency amplitudes. IEEE Access. 2026;14:31856–66. doi:10.1109/ACCESS.2026.3668593.
16. Huang Y, Wu D, Zhang Z, Chen H, Chen S. EMD-based pulsed TIG welding process porosity defect detection and defect diagnosis using GA-SVM. J Mater Process Technol. 2017;239:92–102. doi:10.1016/j.jmatprotec.2016.07.015.
17. Liang S, Chen Y, Liang H, Li X. Sparse representation and SVM diagnosis method for inter-turn short-circuit fault in PMSM. Appl Sci. 2019;9(2):224. doi:10.3390/app9020224.
18. Chauhan S, Vashishtha G, Kumar R, Zimroz R, Gupta MK, Kundu P. An adaptive feature mode decomposition based on a novel health indicator for bearing fault diagnosis. Measurement. 2024;226:114191. doi:10.1016/j.measurement.2024.114191.
19. Mirjalili S. Moth-flame optimization algorithm: a novel nature-inspired heuristic paradigm. Knowl Based Syst. 2015;89:228–49. doi:10.1016/j.knosys.2015.07.006.